Available online at www.sciencedirect.com

ScienceDirect

Procedia Engineering 00 (2015) 1–11

Procedia Engineering

www.elsevier.com/locate/procedia

7th International Conference on Fluid Mechanics, ICFM7

# Large Eddy Simulation of Base Drag Reduction with Jet Boat-Tail Passive Flow Control

Yunchao Yang[a], Heyong Xu[b], Jianlei Wang[b], Ge-Cheng Zha[a,*]

[a]*Department of Mechanical and Aerospace Engineering, University of Miami, Coral Gables, FL*
[b]*School of Aeronautics, Northwestern Polytechnical University, Xi'an,China*

**Abstract**

A Large Eddy Simulation (LES) of base drag reduction for automotive side view mirrors using passive Jet Boat-Tail (JBT) passive flow control is conducted. The JBT passive flow control technique is to introduce a strong jet by opening an inlet in the front of a bluff body, accelerate the jet via a converging duct and eject the jet at an angle toward the center of the base surface. The high speed jet flow entrains the free stream flow to energize the base flow and increase base flow pressure. The LES investigation of flow over a JBT mirror and baseline mirror model is conducted with a low diffusion E-CUSP scheme with fifth order WENO scheme for the inviscid term and fourth order central differencing for the viscous term. The LES calculation indicates that strong passive flow jet enhances the flow entrainment, which mixes with the main flow and transfers the energy from the main stream to the base flow by increasing base flow pressure, thus reducing pressure drag. The preliminary analysis of the flow structures with wake and jet interaction is presented.



*Keywords:* Large eddy simulation, drag reduction, jet-boat-tail passive flow control

## 1. Introduction

Aerodynamic design of automobiles is an important part in designing commercial vehicles with high energy efficiency and low emission. With the typical blunt body shape of road vehicle, reducing base flow drag is a very important issue [1]. Current available methods for drag reduction of bluff bodies include boat-tailing, base-bleed and moving surfaces etc. [2]. Boat-tailing can reduce the drag of tractor-trailer while increasing vehicle length a lot. For the base-bleeding concept, a stream of air is introduced to create extra counter-rotational vortexes in its original wake vortices, by opening a hole at front stagnation point to the rear base surface. This method is rarely used because it impairs the overall design and some functions of the vehicles. A typical moving surfaces control method is emploing rotating cylinders to reduce boundary layer separation [3]. The effectiveness of rotating cylinders on reducing the drag of trucks are verified with wind-tunnel tests. However, the power requirement for the device to rotate the cylinders is probably its limitation.

*Corresponding author. Tel.: +1-305-284-3328 ; fax: +1-305-284-2580.
*Email address:* gzha@miami.edu (Ge-Cheng Zha)

The rear view side mirrors impose a non-negligible contribution to the overall drag of automobiles for their considerable cross-flow dimension and to the high values of their drag coefficient [2]. Usually the aerodynamic drag induced by rear view side mirrors accounts for about 2%-7% of total aerodynamic drag of a vehicle. Recently, a novel Jet-Boat Tail(JBT) control concept is introduced and studied by Zha et al. [4, 5]. As is shown in Fig.1, an accelerated jet is introduced by opening an inlet in the front of the mirror and accelerating the jet via a converging duct. The strong jet exits at an angle toward the center of the base surface, mixes with main stream and produces large vortex structures, which entrain the main flow to the base area and energize the base flow with higher base pressure, thus reduced total pressure drag. Bartow et al. [4] presented a experimental research on two JBT mirror and a baseline models. JBT-1 with smaller inlet area initiates large coherent paired vortex structures and flow entrainment earlier than baseline model while JBT-2 generates inversely paired vortices in the shear layer due to the high jet momentum. Wang et al. [5] measured the drag coefficient of JBT-1 and baseline mirror model. A significant drag reduction is observed from the wind tunnel testing. However, there is still lack of understanding of the mixing mechanism and detailed flow structures on this new JBT passive flow control concept.

In this paper, systematic research on flow structures baseline and JBT-2 mirror models are preformed using high fidelity Large Eddy Simulation . The purpose is to conduct a preliminary investigation in air flow over the JBT mirror and baseline mirror and to explore the drag reduction mechanism with introducing the JBT jet.

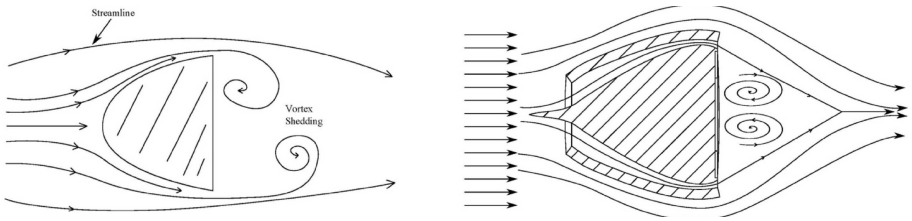


Fig. 1. Typical hypothesized flow structures with conventional car mirror and JBT mirror

## 2. Spatially Filtered Compressible Navier-Stokes Equations

The spatial filtering eliminates the small scale high frequency components of the fluid motion, while keeping the unsteadiness associated with the large scale turbulent motion. For an arbitrary function $u(x_i, t)$, the filtered variable $\bar{u}(x_i, t)$ is defined as:

$$\bar{u}(x_i, t) = \int_D G(x_i - \xi_i, \Delta) u(\xi_i, t) d\xi_i \tag{1}$$

where G is the filter function and $\Delta$ is the filter width and is associated with the mesh size. Similar to the case of RANS, for compressible flows, it is convenient to introduce the Farve-filtered variable $\tilde{u}(x_i, t)$ as:

$$\tilde{u}(x_i, t) = \frac{\overline{\rho u}}{\bar{\rho}} \tag{2}$$

A variable can be thus decomposed into its Favre-filtered component and fluctuating component as:

$$u(x_i, t) = \tilde{u}(x_i, t) + u''(x_i, t) \tag{3}$$

Applying these definitions and following the derivation of Knight et al.[6], the filtered compressible Navier-Stokes(NS) equations in Cartesian coordinates can be expressed as:

$$\frac{\partial \mathbf{Q}}{\partial t} + \frac{\partial \mathbf{E}}{\partial x} + \frac{\partial \mathbf{F}}{\partial y} + \frac{\partial \mathbf{G}}{\partial z} = \frac{1}{Re}\left(\frac{\partial \mathbf{R}}{\partial x} + \frac{\partial \mathbf{S}}{\partial y} + \frac{\partial \mathbf{T}}{\partial z}\right) \tag{4}$$

where

$$\mathbf{Q} = \begin{pmatrix} \bar{\rho} \\ \bar{\rho}\tilde{u} \\ \bar{\rho}\tilde{v} \\ \bar{\rho}\tilde{w} \\ \bar{\rho}\tilde{e} \end{pmatrix}, \mathbf{E} = \begin{pmatrix} \bar{\rho}\tilde{u} \\ \bar{\rho}\tilde{u}^2 + \bar{p} \\ \bar{\rho}\tilde{u}\tilde{v} \\ \bar{\rho}\tilde{u}\tilde{w} \\ (\bar{\rho}\tilde{e} + \bar{p})\tilde{u} \end{pmatrix}, \mathbf{F} = \begin{pmatrix} \bar{\rho}\tilde{v} \\ \bar{\rho}\tilde{v}\tilde{u} \\ \bar{\rho}\tilde{v}^2 + \bar{p} \\ \bar{\rho}\tilde{v}\tilde{w} \\ (\bar{\rho}\tilde{e} + \bar{p})\tilde{v} \end{pmatrix}, \mathbf{G} = \begin{pmatrix} \bar{\rho}\tilde{w} \\ \bar{\rho}\tilde{w}\tilde{u} \\ \bar{\rho}\tilde{w}\tilde{v} \\ \bar{\rho}\tilde{w}^2 + \bar{p} \\ (\bar{\rho}\tilde{e} + \bar{p})\tilde{w} \end{pmatrix}$$

$$\mathbf{R} = \begin{pmatrix} 0 \\ \bar{\tau}_{xx} + \sigma_{xx} \\ \bar{\tau}_{xy} + \sigma_{xy} \\ \bar{\tau}_{xz} + \sigma_{xz} \\ Q_x \end{pmatrix}, \mathbf{S} = \begin{pmatrix} 0 \\ \bar{\tau}_{yx} + \sigma_{yx} \\ \bar{\tau}_{yy} + \sigma_{yy} \\ \bar{\tau}_{yz} + \sigma_{yz} \\ Q_y \end{pmatrix}, \mathbf{T} = \begin{pmatrix} 0 \\ \bar{\tau}_{zx} + \sigma_{zx} \\ \bar{\tau}_{zy} + \sigma_{zy} \\ \bar{\tau}_{zz} + \sigma_{zz} \\ Q_z \end{pmatrix}$$

The overbar denotes a regular filtered variable as given in eq. (1), and the tilde is used to denote the Favre filtered variable defined in eq. (2). In above equations, $\rho$ is the density, $u, v, w$ are the Cartesian velocity components in $x, y, z$ directions, $p$ is the static pressure, and $e$ is the total energy per unit mass.

The $\bar{\tau}$ is the molecular viscous stress tensor and is estimated as:

$$\bar{\tau}_{ij} = \frac{2}{3}\tilde{\mu}\frac{\partial \tilde{u}_k}{\partial x}_k \delta_{ij} + \tilde{\mu}(\frac{\partial \tilde{u}_i}{\partial x_j} + \frac{\partial \tilde{u}_j}{\partial x_i}), \quad i, j = 1, 2, 3 \tag{5}$$

The above equation is in the tensor form, where the subscript 1, 2, 3 represent the coordinates, $x, y, z$ and the Einstein summation convention is used. The molecular viscosity $\tilde{\mu} = \tilde{\mu}(\tilde{T})$ is determined by Sutherland law.

The $\sigma$ is the subgrid-scale(SGS) stress tensor due to the filtering process and is expressed as:

$$\sigma_{ij} = -\bar{\rho}(\widetilde{u_i u_j} - \tilde{u}_i \tilde{u}_j) \tag{6}$$

The energy flux $Q_i$ is expressed as:

$$Q_i = \tilde{u}_j(\bar{\tau}_{ij} + \sigma_{ij}) - \bar{q}_i + \Phi_i \tag{7}$$

where $\Phi_i$ is the subscale heat flux, $\bar{q}_i$ is the molecular heat flux.

The implicit LES strategy for the closure of the SGS stress tensor and the energy flux adopted in [7, 8] is also employed in this research.

**In generalized coordinates**$(\xi, \eta, \zeta)$, the governing Eq.(4) can be expressed as the following conservative form:

$$\frac{\partial Q}{\partial t} + \frac{\partial E}{\partial \xi} + \frac{\partial F}{\partial \eta} + \frac{\partial G}{\partial \zeta} = \frac{1}{Re}\left(\frac{\partial R}{\partial \xi} + \frac{\partial S}{\partial \eta} + \frac{\partial T}{\partial \zeta}\right) \tag{8}$$

where $Re$ is the Reynolds number. The conservative variable vector $Q$, the inviscid flux vectors $E, F, G$, and the viscous fluxs $R, S, T$ are expressed as

$$Q = \frac{1}{J}\begin{pmatrix} \bar{\rho} \\ \bar{\rho}\tilde{u} \\ \bar{\rho}\tilde{v} \\ \bar{\rho}\tilde{w} \\ \bar{\rho}\tilde{e} \end{pmatrix}, E = \begin{pmatrix} \bar{\rho}U \\ \bar{\rho}\tilde{u}U + l_x\bar{p} \\ \bar{\rho}\tilde{v}U + l_y\bar{p} \\ \bar{\rho}\tilde{w}U + l_z\bar{p} \end{pmatrix}, F = \begin{pmatrix} \bar{\rho}V \\ \bar{\rho}\tilde{u}V + m_x\bar{p} \\ \bar{\rho}\tilde{v}V + m_y\bar{p} \\ \bar{\rho}\tilde{w}V + m_z\bar{p} \end{pmatrix}, G = \begin{pmatrix} \bar{\rho}W \\ \bar{\rho}\tilde{u}W + n_x\bar{p} \\ \bar{\rho}\tilde{v}W + n_y\bar{p} \\ \bar{\rho}\tilde{w}W + n_z\bar{p} \end{pmatrix}$$

$$R = \begin{pmatrix} 0 \\ l_k\bar{\tau}_{xk} \\ l_k\bar{\tau}_{yk} \\ l_k\bar{\tau}_{zk} \\ l_k\left(\tilde{u}_i\bar{\tau}_{ki} - \bar{q}_k\right) \end{pmatrix}, S = \begin{pmatrix} 0 \\ m_k\bar{\tau}u_{xk} \\ m_k\bar{\tau}_{yk} \\ m_k\bar{\tau}u_{zk} \\ m_k\left(\tilde{u}_i\bar{\tau}_{ki} - \bar{q}_k\right) \end{pmatrix}, T = \begin{pmatrix} 0 \\ n_k\bar{\tau}_{xk} \\ n_k\bar{\tau}_{yk} \\ n_k\bar{\tau}_{zk} \\ n_k\left(\tilde{u}_i\bar{\tau}_{ki} - \bar{q}_k\right) \end{pmatrix}$$

where $U$, $V$ and $W$ are the contravariant velocities in $\xi$, $\eta$, $\zeta$ directions, and defined as follows.

$$U = l_t + \mathbf{l} \bullet \mathbf{V} = l_t + l_x\tilde{u} + l_y\tilde{v} + l_z\tilde{w} \tag{9}$$

$$V = m_t + \mathbf{m} \bullet \mathbf{V} = m_t + m_x\tilde{u} + m_y\tilde{v} + m_z\tilde{w} \tag{10}$$

$$W = n_t + \mathbf{n} \bullet \mathbf{V} = n_t + n_x\tilde{u} + n_y\tilde{v} + n_z\tilde{w} \tag{11}$$

where $l_t$, $m_t$ and $n_t$ are the components of the interface contravariant velocity of the control volume in $\xi$, $\eta$ and $\zeta$ directions respectively. $\mathbf{l}$, $\mathbf{m}$ and $\mathbf{n}$ denote the normal vectors located at the centers of $\xi$, $\eta$ and $\zeta$ interfaces of the control volume with their magnitudes equal to the surface areas and pointing to the directions of increasing $\xi$, $\eta$ and $\zeta$. $J$ is the Jacobian of the transformation.

### *2.1. The Low Diffusion E-CUSP (LDE) Scheme*

The LDE scheme developed by Zha et al [9] is employed to evaluate the inviscid fluxes. The basic idea of the LDE scheme is to split the inviscid flux into the convective flux $E^c$ and the pressure flux $E^p$. Even with the one extra equation from the S-A model, the splitting is basically the same as the original scheme for the Euler equation and is straightforward. This is an advantage over the Roe scheme, for which the eigenvectors need to be derived when any extra equation is added to the governing equations.

In generalized coordinate system, the flux $\mathbf{E}$ can be split as the following:

$$\mathbf{E} = E^c + E^p = \begin{pmatrix} \rho U \\ \rho u U \\ \rho v U \\ \rho w U \\ \rho e U \end{pmatrix} + \begin{pmatrix} 0 \\ l_x p \\ l_y p \\ l_z p \\ p\overline{U} \end{pmatrix}, \tag{12}$$

### *2.2. The Fifth-Order WENO Scheme*

The interface flux, $E_{i+\frac{1}{2}} = E(Q_L, Q_R)$, is evaluated by determining the conservative variables $Q_L$ and $Q_R$ using fifth-order finite difference WENO scheme [[10] and [11]]. For example,

$$(Q_L)_{i+\frac{1}{2}} = \omega_0 q_0 + \omega_1 q_1 + \omega_2 q_2, \tag{13}$$

where

$$\begin{aligned} q_0 &= \tfrac{1}{3}Q_{i-2} - \tfrac{7}{6}Q_{i-1} + \tfrac{11}{6}Q_i, \\ q_1 &= -\tfrac{1}{6}Q_{i-1} + \tfrac{5}{6}Q_i + \tfrac{1}{3}Q_{i+1}, \\ q_2 &= \tfrac{1}{3}Q_i + \tfrac{5}{6}Q_{i+1} - \tfrac{1}{6}Q_{i+2}, \end{aligned} \tag{14}$$

The viscous terms are discretized by a fully conservative fourth-order accurate finite central differencing scheme[12].

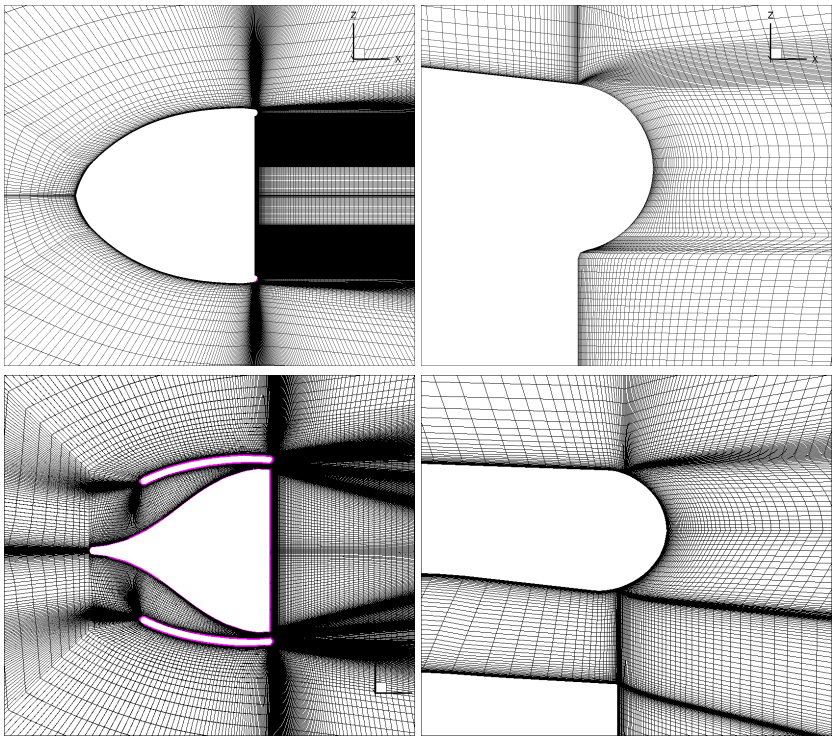

Fig. 2. Cross-section mesh of baseline and JBT model

### 2.3. Implicit Time Integration

The time dependent governing equations are solved using dual time stepping method suggested by Jameson[13]. To achieve high convergence rate, the implicit pseudo time marching scheme is used with the unfactored Gauss-Seidel line relaxation. The physical temporal term is discretized implicitly using a three point, backward differencing as the following:

$$\frac{\partial Q}{\partial t} = \frac{3Q^{n+1} - 4Q^n + Q^{n-1}}{2\Delta t}, \tag{15}$$

where $n-1$, $n$ and $n+1$ are three sequential time levels, which have a time interval of $\Delta t$. The first-order Euler scheme is used to discretize the pseudo temporal term. The semi-discretized equations of the governing equations are finally given as the following:

$$\left[\left(\frac{1}{\Delta\tau} + \frac{1.5}{\Delta t}\right) I - \left(\frac{\partial R}{\partial Q}\right)^{n+1,m}\right] \delta Q^{n+1,m+1} = R^{n+1,m} - \frac{3Q^{n+1,m} - 4Q^n + Q^{n-1}}{2\Delta t}, \tag{16}$$

where the $\Delta\tau$ is the pseudo time step, R is the net flux evaluated on a grid point using the fifth-order finite difference WENO scheme for the inviscid fluxes and the fourth-order central differencing scheme for the viscous terms [10, 12, 11].

## 3. Simulation Setup

The baseline and JBT mirror configurations are described in the paper by Wang et al [5]. Simulations are conducted with the same free stream speed of 30 m/s and Reynolds number of $2.56 \times 10^5$ based on the baseline mirror length. Far field boundary is set at 80 times characteristic length of baseline mirror model.

The no-slip boundary condition is applied on all the wall surfaces. Two multiblock structured meshes are generated for the LES calculations as shown in Fig. 2. For the baseline model, a mesh of 28.86 million cells is generated with very fine mesh in the wake region. For the JBT model, a mesh of 25.94 million cells is generated, with refined mesh near the tunnel region and wake region. The $y_1^+$ is calculated from the normal distance of the first wall grid and is mostly less than 1, as shown in Fig. 3. The JBT mirror model has the same external shape as the baseline model except that the JBT model has the front part cut off to create an inlet opening. The non-dimensional time step used is 0.02.

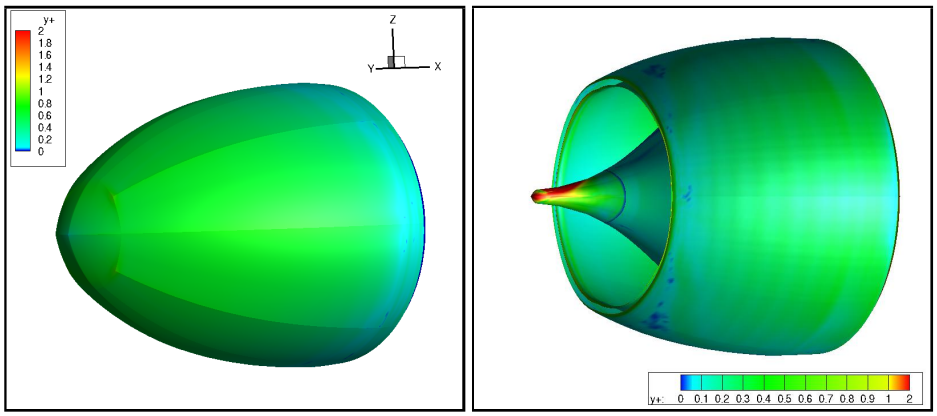


Fig. 3. Caculated surface mesh first normal distance of baseline and JBT model

## 4. Results and Discussion

The comparison of simulation results with experiments are shown in Table 1. The calculated baseline model drag coefficient agrees well with the measurements while the simulated JBT model drag coefficient is overpredicted by 23.9%.

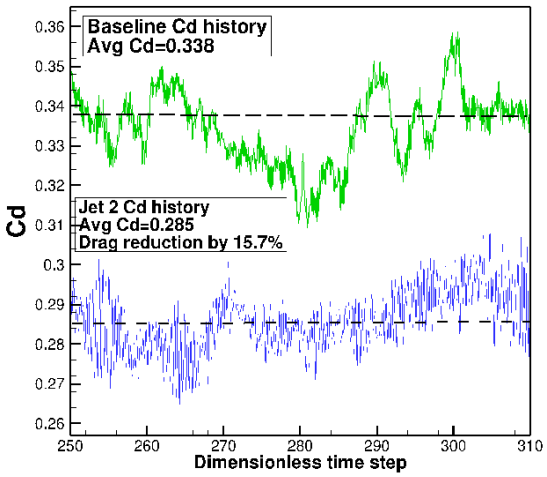


Fig. 4. Drag coefficient Cd history in the LES calculation

Drag coefficient history from LES is presented from dimensionless time 250 to 310 in Fig 4. Calculated drag coefficients of baseline and JBT oscillate due to vortex shedding and shear layer instability. Sixty di-

Table 1. Drag coefficient comparison between simulation and experiment

| Exp. Point | Baseline | JBT | Drag Reduction (%) |
|---|---|---|---|
| Cd_exp. | 0.31 | 0.23 | 25.8% |
| Cd_sim. | 0.338 | 0.285 | 15.6% |
| Discrepancy(%) | 9% | 23.9% | 39.5% |

mensionless time steps are used to obtain the time-average drag coefficient.

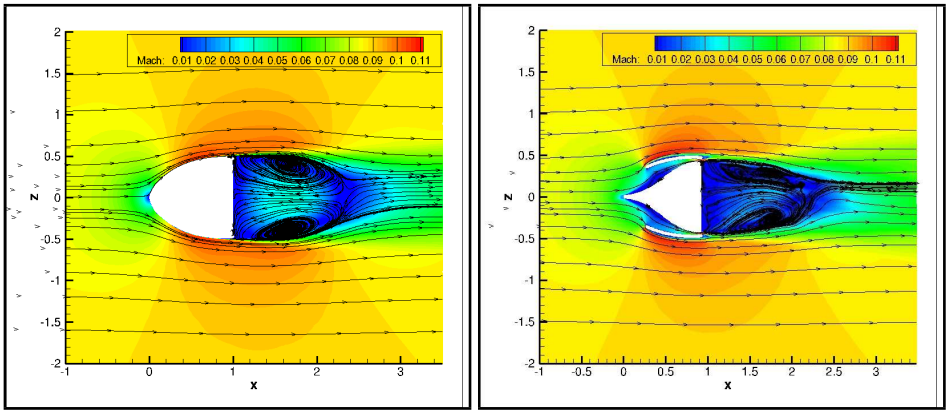


Fig. 5. Time-averaged streamline of baseline and JBT mirror

The time-averaged flow streamline in Fig. 5 show a typical bluff body flow structure with a recirculation in the wake with two counter-rotational vortexes. It is clearly seen that the zero-velocity-streamline enclosing the circulation zone of the JBT model converges earlier than the baseline model. The speed at the exit of tunnel reaches Mach number 0.13 as shown in Fig. 6, which is much higher than the free stream Mach number of 0.08. The strong jet is important to enhance the entrainment by interacting with the shear layer from the shell.

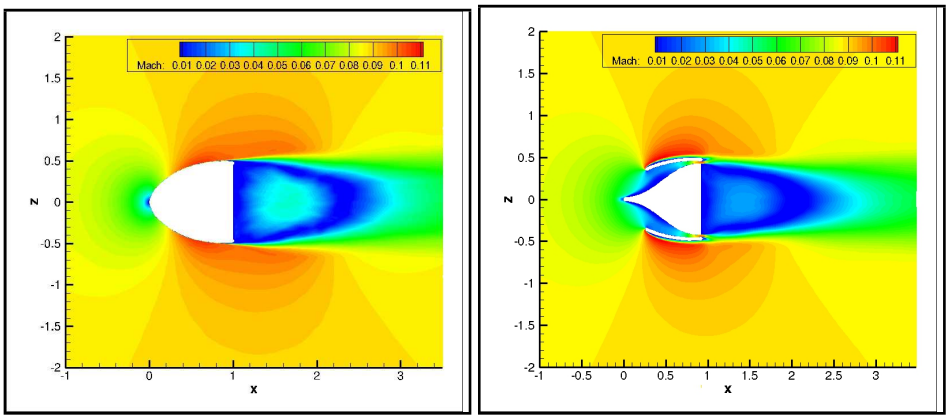


Fig. 6. Time-averaged mach number of baseline and JBT mirror

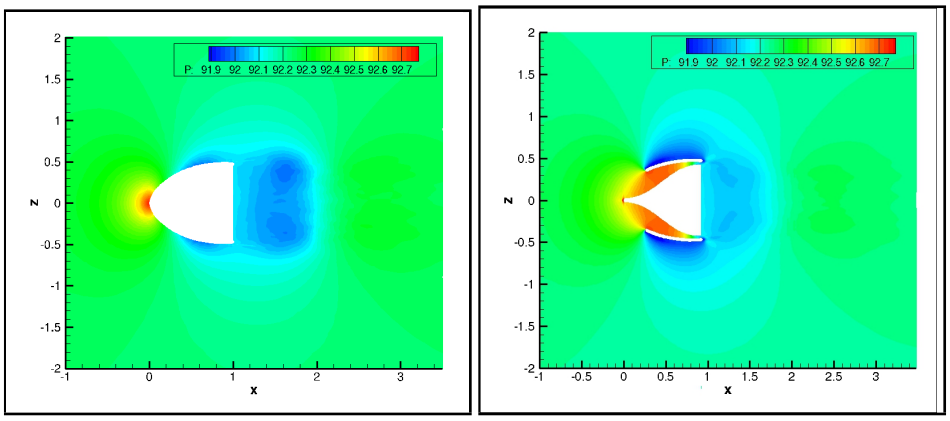


Fig. 7. Time-averaged static pressure of baseline and JBT mirror

Fig. 7 shows the time-averaged static pressure field of the baseline and JBT model flow field. The pressure in the base region of the JBT model is significantly higher than that of the baseline model and thus generates lower pressure drag. The static pressure on the shell surface is lower than that of the baseline due to higher flow acceleration induced by the jet.

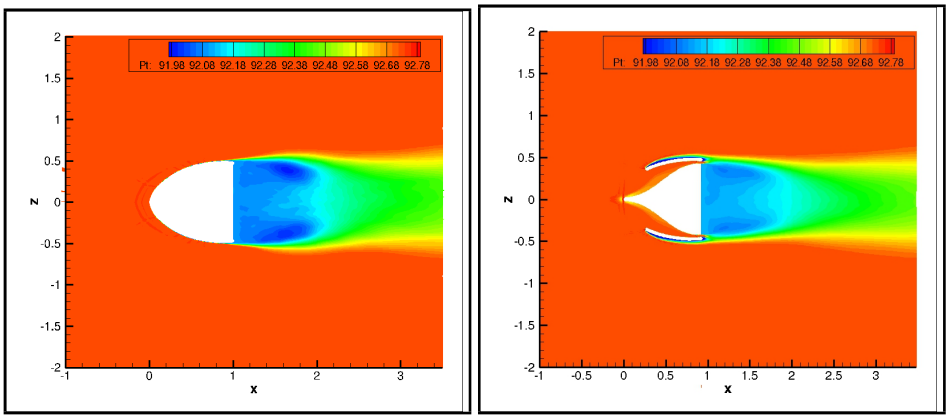


Fig. 8. Time-averaged total pressure of baseline and JBT mirror

Fig. 8 illustrates the time-averaged total pressure field of the baseline and JBT model flow field. It is quite clear that total pressure loss in the base region of baseline model is much larger than that of the JBT model. It indicates that total pressure loss of flow over the JBT model is less than baseline due to the jet entrainment that transfers energy from the free stream to low pressure base flow region.

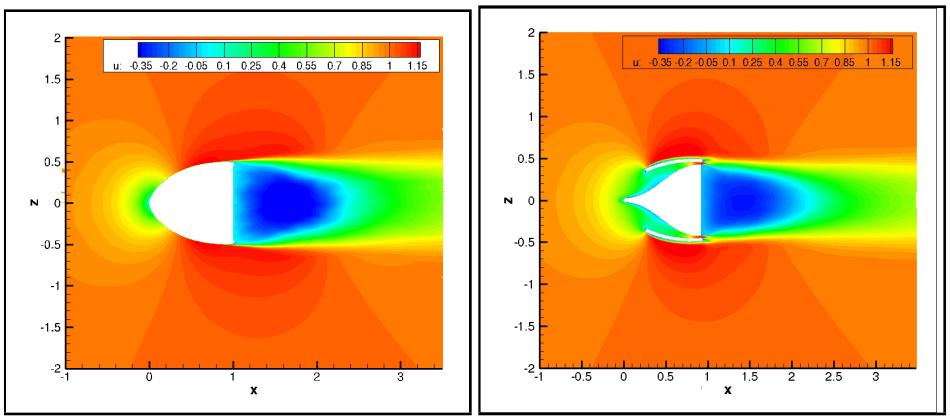


Fig. 9. Time-averaged x-componet velocity of baseline and JBT mirror

Fig. 9 is the time-averaged streamwise velocity component (x-component, u) contours of the baseline and JBT model. In the streamwise velocity contours, significantly narrowed blue and green regions along the flow path is observed in flow over JBT mirror, indicating smaller wake velocity deficit in the base flow region. Flow speed at the jet exit is very high than its neighboring area.

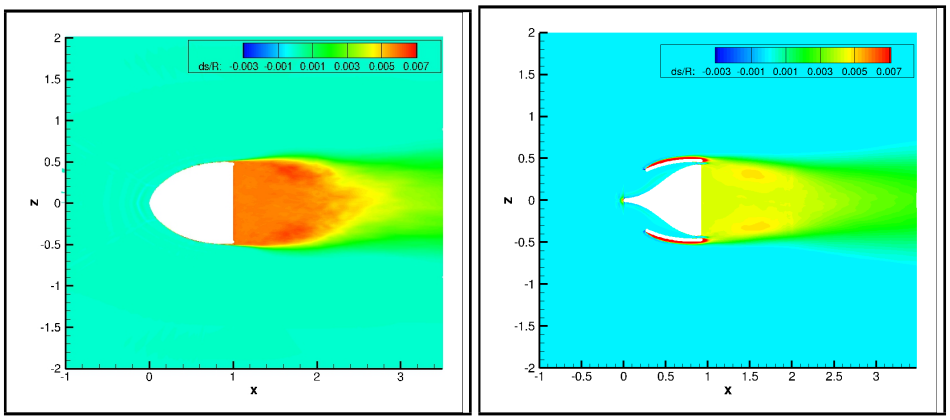


Fig. 10. Time-averaged entropy of baseline and JBT mirror

Fig. 10 displays time-averaged flow entropy production at the mid-plane of baseline model and JBT model. It can be seen that the entropy production of red base region of baseline mirror is clear much larger than that of the yellow base region of JBT mirror model. Higher entropy production indicates that flow over the JBT model undergoes less energy loss in the base region.

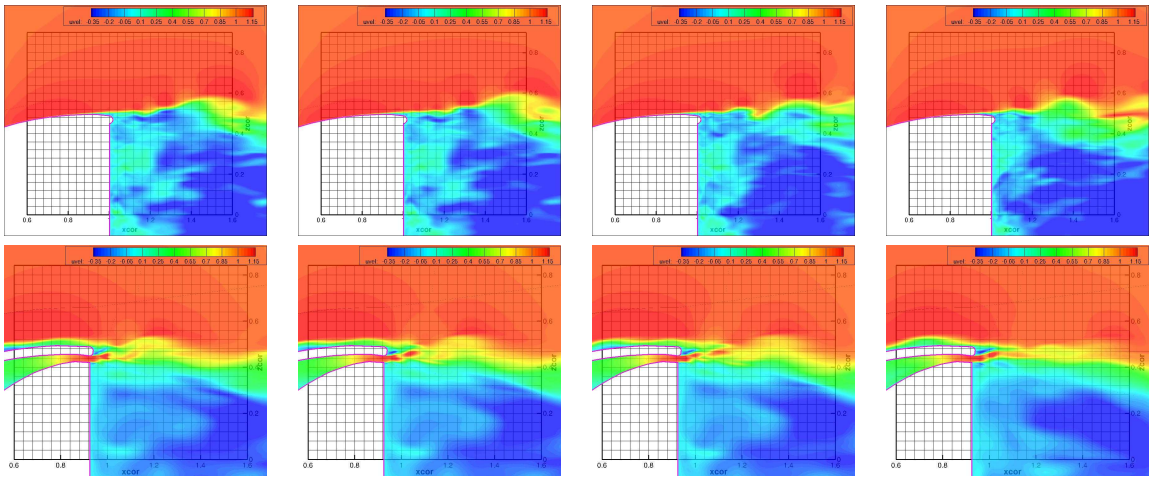


Fig. 11. Instaneous x-componet velocity contours at the tip of baseline and JBT model

Instantaneous streamwise velocity contours are displayed in Fig. 11. The shear layer of the baseline model is more opened up going downstream whereas the JBT wake is more converging with the reduced width. The same trend is also shown in the instantaneous vorticity contours in Fig. 12. It is clearly that the coherent vortex structures in the shear layer emanating from the wall surface of the baseline mirror. The baseline base flow is dominated by small flow structures and chaotic turbulent flow. Larger flow structures are discovered in the JBT base flow area with the vortex paring in the shear layer. In the JBT base region, the dominant vortex structures are much larger than those of the baseline model, conveying a stronger entrainment effect from the main stream to the base region.

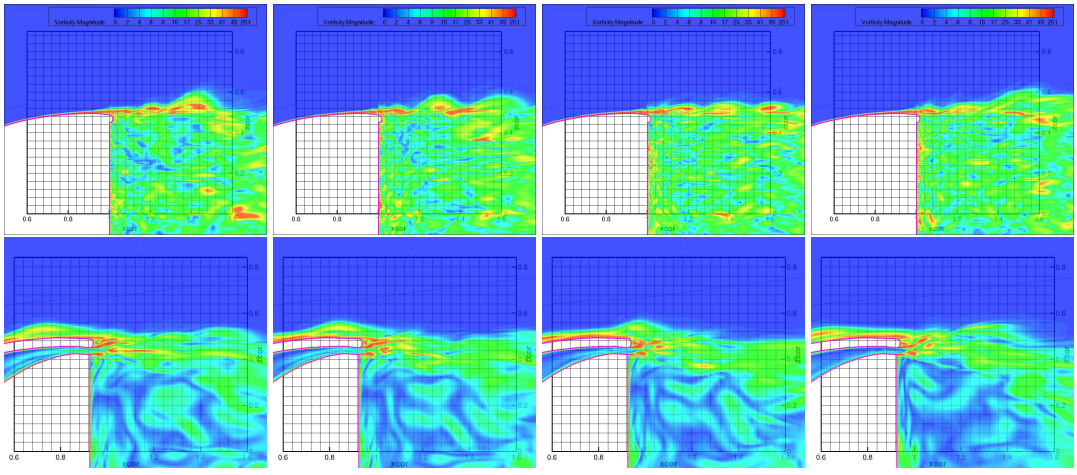

Fig. 12. Instaneous vorticity contours at the tip of baseline and JBT model

## 5. Conclusion

In this paper, a preliminary analysis of LES investigation of drag reduction mechanism of JBT passive flow control concept is performed. LES calculation indicates that the JBT technique is very effective to reduce base flow drag on automobile rear-view mirrors. It is also clear that the introduced passive jet enhances the flow entrainment, which mixes with the main flow and transfers the energy from the main stream to the

base flow by increasing base flow pressure, accordingly reducing pressure drag. High speed jet interaction with the shear layer enhances the flow entrainment and mixing by generating vortex pairing. The baseline base flow is dominated by chaotic turbulence, while Large flow structures are observed in the JBT base flow area.

## 6. Acknowledgement

The computation is conducted at the Oak Ridge National Lab super-computing center and the Center for Computational Sciences at the University of Miami. We would also like to show our gratitude to the sponsor of University of Miami GAFAC Committee.

## References

[1] W.-h. Hucho and G. Sovran, "Aerodynamics of road vehicles," *Annual review of fluid mechanics*, vol. 25, no. 1, pp. 485–537, 1993.
[2] G. Buresti, G. Iungo, and G. Lombardi, "Methods for the drag reduction of bluff bodies and their application to heavy road-vehicles," *1st Interim Report Contract between CRF and DIA, DDIA2007-6*, 2007.
[3] V. Modi, "Moving surface boundary-layer control: A review," *Journal of Fluids and Structures*, vol. 11, no. 6, pp. 627–663, 1997.
[4] W. B. Bartow, A. C. Moreyra, T. Hirst, G. H. Woyczynski, A. Lefebvre, and G. Zha, "Experimental investigations of vehicle base drag reduction using passive jet boat-tail flow control," tech. rep., SAE Technical Paper, 2014.
[5] J. Wang, W. Bartow, A. Moreyra, G. Woyczynski, A. Lefebvre, E. Carrington, and G. Zha, "Low drag automotive mirrors using passive jet flow control," tech. rep., SAE Technical Paper, 2014.
[6] D. Knight, G. Zhou, N. Okong'o, and V. Shukla, "Compressible Large Eddy Simulation Using Unstructured Grids." AIAA Paper 98-0535, 1998.
[7] Shen, Y.-Q. and Zha, G.-C.
[8] H.-S. Im, G.-C. Zha, and B. P. Dano, "Large eddy simulation of coflow jet airfoil at high angle of attack," *Journal of Fluids Engineering*, vol. 136, no. 2, p. 021101, 2014.
[9] G.-C. Zha, Y. Shen, and B. Wang, "An improved low diffusion E-CUSP upwind scheme ," *Journal of Computer & Fluids*, vol. 48, pp. 214–220, 2011.
[10] Shen, Y.-Q. and Zha, G.-C. and Wang, B.-Y., " Improvement of Stability and Accuracy of Implicit WENO Scheme," *AIAA Journal*, vol. 47, No. 2, pp. 331–344, 2009.
[11] Shen, Y.-Q. and Zha, G.-C. , " Improvement of the WENO Scheme Smoothness Estimator," *International Journal for Numerical Methods in Fluids*, vol. DOI:10.1002/fld.2186, 2009.
[12] Shen, Y.-Q. and Zha, G.-C. and Chen, X.-Y., " High Order Conservative Differencing for Viscous Terms and the Application to Vortex-Induced Vibration Flows," *Journal of Computational Physics*, vol. 228(2), pp. 8283–8300, 2009.
[13] A. Jameson, "Time Dependent Calculations Using Multigrid with Application to Unsteady Flows past Airfoils and Wings." AIAA Paper 91-1596, 1991.